TÜBİTAK

Turk J Elec Eng & Comp Sci, Vol.19, No.3, 2011, © TÜBİTAK
doi:10.3906/elk-0905-28

Obtaining the secondary impedance of single-sided linear induction motor with a double layer reaction rail: a new approach

Ali Suat GERÇEK, Vedat Mehmet KARSLI*
Department of Electrical-Electronics Engineering, Gaziantep University, Gaziantep-TURKEY
e-mail: gercek@gantep.edu.tr, vkarsli@gantep.edu.tr

Received: 04.05.2009

Abstract

In the performance calculations of single-sided linear induction motor (SLIM),the equivalent circuit technique (ECT) is used. In this paper, a new approach is proposed for obtaining the secondary impedance of single-sided linear induction motor (SLIM) with a double layer reaction rail by using the layered secondary model. The proposed method improves the ECT technique by considering the saturation effect and the non-linear complex equivalent relative permeability. This study also examines the contributions of other electromagnetic effects, such as longitudinal end effect and transverse edge effect as well. Our method is applied to the SLIM and computed results of the method are compared to the experimental results of the previous studies. This evaluation proved that the outcomes of the proposed method are in accordance with the experimental results widely studied in the literature.

Key Words: *Linear induction motor, secondary impedance, least square*

1. Introduction

Single-sided linear induction motors (SLIM) are widely utilized in industrial applications and transportation due to their simple structure, ease of implementation in manufacturing, high reliability and speed, low energy consumption and pollution [1]. Generally, a double layer reaction rail SLIM is made up of two major parts: a primary and a secondary. The primary consists of slots which hold primary windings. The secondary of the SLIM holds a conducting plate which is backed by a ferromagnetic material, "back iron" or "secondary iron" [2]. While the motor operates, some essential electromagnetic phenomena occur because of the structure of the motor and its physical properties. To take into account these phenomena in performance calculations, several corrections should be introduced thereafter in the form of reiterated calculations or of correction factors [3].

The equivalent circuit technique (ECT) is assessed numerous studies [1–4] in the literature and it is shown that the method is appropriate to utilize the ECT for the steady state performance calculation of the SLIM where particularly the T-type equivalent circuit is usually preferred. In order to employ the T-type equivalent circuit,

*Corresponding author: Department of Electrical-Electronics Engineering, Gaziantep University, Gaziantep-TURKEY

primary resistance, primary reactance, magnetizing branch, magnetizing reactance and secondary impedance should be considered. The magnetizing branch reactance and secondary impedance are obtained by solving the field equations which are acquired from the electromagnetic field analysis through the layer method. Although, the layer method is widely used for the electromagnetic analysis of the SLIM [5, 6], the analytic results obtained via this method are not adequately close to the values measured over a wide range of operating conditions. The main reason for the mentioned problem is actually the inadequate treatment of the saturation effect and the depth of penetration, which is related to the permeability of the secondary iron, in the back iron for high frequency applications. An adequate consideration of such parameters in addition to the others will provide the correct calculation of the secondary impedance; moreover, it will present more precise performance prediction for both analysis and design stages as well. Thus, research over the mentioned problem is still essential.

For this purpose, in this paper, the following tasks are performed: a) Layered secondary model together with the special phenomena is presented, b) Saturation level of the back iron is determined by iteration. Having accomplished aforementioned tasks, we calculate secondary iron impedance by using a linear approximation that is novel in the calculation of secondary iron impedance. The developed model with this novel approach is then applied to the Canadian Guided Ground Transportation (CIGGT) LIM to assess its performance under the above mentioned conditions, e.g., high frequency drawbacks. The results are compared with those given in the experiments of the previous studies.

2. Special phenomena in SLIM

In the layer method, primary current represents the line current density J_{ex} and secondary comprises an aluminum cap over solid steel core. Figure 1 shows the provision of the layers in a linear induction motor supplied with a sinusoidal power source:

$$J_{ex} = Re\left\{J_{ex}\exp\left[j\left(\omega t - kx\right)\right]\right\}. \tag{1}$$

Here, $k{=}2\pi/\lambda$.

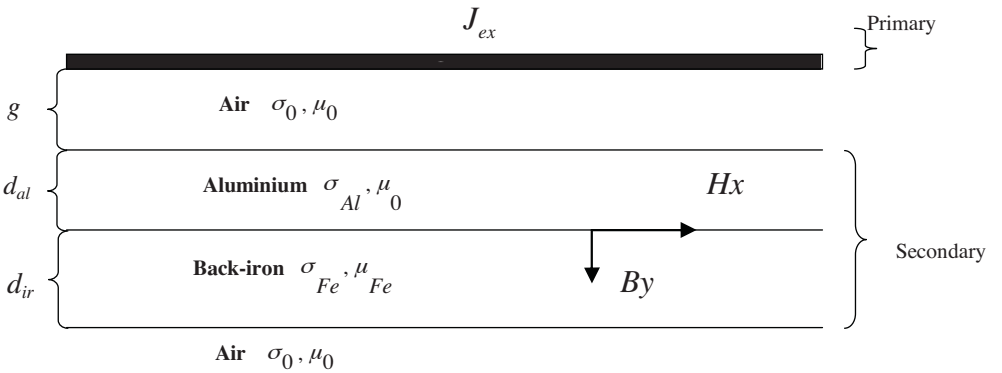

Figure 1. Basic layering model of SLIM with double layer reaction rail in longitudinal section.

The electromagnetic field is supposed invariant in the transverse direction (z) and there are no specific paths for induced current in the secondary [2]. The effect of this current, which is known as transverse edge effect, is taken into account by adjusting the conductivity of the conducting plate with the Russels and Norsworthy corrected factor k_{RN} [7]:

$$\sigma'_{A1} = k_{RN}\sigma_{A1}. \tag{2}$$

The Longitudinal end effects in the linear induction motor are due to the limiting longitudinal length of the motor. It influences the speed on the non uniform distribution of the induction in the air gap of the LIM and current induced in the secondary. This effect is taken into account by a factor k_e given on the basis of a distribution of induction in the air gap of SLIM made up of a slipping field. The end effect can be expressed as a summation of two air gap flux density waves [1]:

$$B(x,t) = B_{ms}\sin(\omega t - \frac{\pi}{\tau}x) + B_{me}e^{-\frac{x}{t_e}}\sin(\omega t - \frac{\pi}{\tau_e}x + \delta). \tag{3}$$

The electromotive force induced in a primary phase is the superposition of two electromotive forces, one due to the fundamental field and the other is induction due to the end effect and it can be expressed in the form [8]

$$e_p(t) = e_s(t) + e_e(t) = -E_{ms}\cos(\omega t) - E_{me}\cos(\omega t) = -E_{ms}(1-ke)\cos(\omega t) \tag{4}$$

where

$$ke = -\frac{k_{we}}{k_w}\frac{\frac{\pi}{\tau_e^2}}{\frac{1}{t_e^2}+\left(\frac{\pi}{\tau_e}\right)^2}f(\delta)e^{\frac{-p\tau_e}{t_e}}\frac{\sinh\left(\frac{p\tau_e}{t_e}\right)}{p\sinh\left(\frac{\tau_e}{t_e}\right)} \quad . \tag{5}$$

Since the ferromagnetic material (back iron) exists in the secondary, the saturation should be considered at some operating conditions. The classical theory of the electric motors defines the saturation factor of the magnetic circuit as being the relationship between the total magneto motive force and that of the air gap by pole pairs. The magnetic permeability of the primary is assumed infinite. So the magneto motive force in the primary can be neglected. Under this condition, the saturation factor of the magnetic circuit of SLIM can be expressed as [9].

$$k_\mu = \frac{V_v}{2\left(V_{gv}+V_{dv}\right)} \approx 1 + \frac{V_{sv}}{2\left(V_{gv}+V_{dv}\right)}, \tag{6}$$

where V_v is the magneto motive force (MMF) per poles pair, V_{gv} is the magnetic voltage drop in the air gap, V_{dv} is the magnetic voltage drop in the conducting plate, and V_{sv} is the magnetic voltage drop in the secondary back iron.

Additionally, the Carter coefficient k_c, which takes the effect of the slot of the primary account and the saturation factor of k_μ, which takes saturation of ferromagnetic secondary account, are employed in order to obtain the equivalent air-gap value [9]

$$g' = k_c k_\mu g. \tag{7}$$

The effects of the saturation and the hysteresis are included into calculation by use of an equivalent relative magnetic permeability of the steel of the secondary, expressed by the relationship [10]

$$\mu_{re} = \mu_{rs}\left(\mu' - j\mu''\right), \tag{8}$$

where μ_{rs} is the permeability that is related to surface of the secondary steel on the side of the primary. The real and imaginary components are described in [10], and are given as

$$\mu' = a_R a_x, \quad \mu'' = 0.5\left(a_R^2 - a_x^2\right), \tag{9}$$

where the coefficients a_R and a_x depend on the magnetic field that exist on the surface of the steel of the secondary. The mentioned coefficients provide the consideration of the saturation and the effect of hysteresis for the purpose of being precise.

3. Wave Penetration depth concept

Anticipating the performance of the SLIM has been carried out via electromagnetic field analysis together with the ECT, which include special phenomena (transverse edge effect, longitudinal end effect, saturation, hysteresis and non-linear complex magnetic permeability) presented in section 2. In ECT, the secondary parameters are evaluated from two dimensional (2-D) field analyses. Thereby, the layering model has been developed by paralleling the layer impedances (as shown in Figure 1) of the motor, considering the wave impedance concept [11].

In the layering model, the secondary iron has two regions: the conducting surface ferromagnet, which has the uniform field distribution in the normal direction (y), and the nonconducting ferromagnet. As per the wave penetration concept, a wave of frequency f penetrates into the layers of the secondary iron having permeability μ and conductivity σ, where the amount of penetration depth is calculated according to equation 15. Thus the thickness of the conducting surface region is assumed to be equal to the penetration depth of the wave, in accordance with the wave penetration concept. It is observed that the penetration depth increases as the secondary frequency (sf) decreases. Note that, the average distance value of flux penetration is limited to be the half of the layer thickness even though the penetration depth value is calculated to be greater than the half of the layer thickness of the secondary iron $(d_{ir}/2)$ as illustrated in Figure 2.

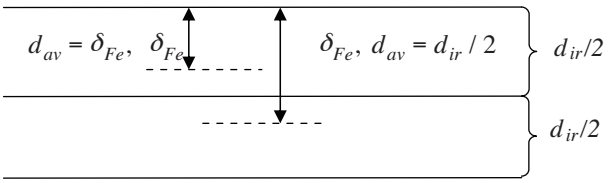

Figure 2. Back iron half space layer modeling.

4. Calculation of saturation level

The following iterative algorithm is used to obtain equivalent magnetic permeability of the back iron, in other words, the saturation level.

- Assumed that the surface magnetic field intensity H_{s1} at the boundary between the solid iron and the aluminum is equal to the line current density of the primary:

$$H_{s1} = A_m = \frac{3\sqrt{2}k_w NI}{p\tau}, \tag{10}$$

  and the saturation factor is assumed k_μ to be equal to one.

- Extract the surface permeability of the back iron from $B - H$ curve data and calculate the equivalent magnetic permeability by using equations (8) and (9).

- Then, the effective air gap $g\prime$ (see equation (7)) and the attenuation factors α_1, α_2 and the propagation constants K_1, K_2 are calculated by using the following expressions [3]:

$$K_1 = \sqrt{\alpha_1^2 + \beta^2} \tag{11}$$

$$K_2 = \sqrt{\alpha_2^2 + \beta^2} \tag{12}$$

$$\alpha_1 = \sqrt{j2\pi f s \mu_0 \mu_{re} \sigma_{Fe}} \tag{13}$$

$$\alpha_2 = \sqrt{j2\pi f s \mu_0 \sigma'_{Al}}, \tag{14}$$

where $\beta = \frac{\pi}{\tau}$.

- Next, in order to determine effective depth d_{av} of the induced currents in the secondary iron layer, the penetration depth of magnetic flux into the back iron is calculated by using the equations [12]

$$\delta_{Fe} = \frac{1}{\sqrt{\pi f s \mu_0 \mu_{rs} \sigma_{Fe}}} \tag{15}$$

$$d_{av} = \begin{cases} \delta_{Fe} & \text{if} \quad \delta_{Fe} < 0.5 d_{ir}, \\ 0.5 d_{ir} & \text{if} \quad \delta_{Fe} > 0.5 d_{ir}. \end{cases} \tag{16}$$

- Later, tangential and normal magnetic field intensity is calculated by the use of (17) to obtain the average magnetic permeability μ_{av} from the $B - H$ curve data of the back iron:

$$H_x = -\frac{K_1 A_m}{M\beta} e^{-j\beta x} e^{-K_1 (y - d_{Al} - g')} \Big|_{y = g + d_{Al} + d_{av}} \tag{17}$$

$$H_y = -\frac{jA_m}{M} - e^{j\beta x} e^{-K_1 (y - d_{Al} - g')} \Big|_{y = g + d_{Al} + d_{av}}, \tag{18}$$

where M is the factor required for the two dimensional analysis of SLIM [3].

- The new saturation factor is then calculated by equation (6).

- In the last step, the magnetic field intensity H_{s2} value at the surface of the back iron is updated by using (17) and (19) with $y = g + d_{Al}$. The above mentioned computation are carried out until a sufficient convergence between H_{s1} and H_{s2} is attained, where each of the magnetic field intensity values can be calculated with the relation

$$H_{s2} = (H_x^2 + H_y^2)^{1/2}. \tag{19}$$

As a consequence of the iterations, the saturation level is determined for each slip value with the consideration of the nonlinear characteristics of the secondary iron as mentioned above. Through the iterations the wave penetration depth is calculated according to the wave penetration depth concept which is explained in Section 3.

5. Simulating the CIGGT SLIM

For the CIGGT SLIM with the given design data in Table 1, the variation of the wave penetration depth with linear speed at different input frequencies (f) is shown in Figure 3. As expected, the depth of the penetration into the secondary iron increases as the slip decreases.

Table 1. Data on CIGGT LIM.

Number of Phase, m	3
Number of pole pairs, p	3
Rated phase current, I	200 A
Pole pitch,τ	25 cm
Air gap length, g	1.5 cm
Number of primary turn/phase, N	108
Width of the aluminum layer, $W + 2h_{ov}$	20.1 cm
Width of the secondary iron layer, W	11.1 cm
Thickness of the aluminum layer, d_{Al}	0.25 cm
Thickness of the secondary iron layer, d_{ir}	2.54 cm
Conductivity of secondary iron, σ_{Fe}	4.46 MS/m
Conductivity of secondary iron, σ_{Al}	32.3 MS/m

The penetration depth, which is dependent on frequency of the secondary, increases to the half the layer thickness at *about the synchronous speed*. The thickness of the conductance path, on which the induced current in the secondary iron flows, also increases with the penetration depth. This thickness should be fixed to a certain value according to the wave impedance concept.

The changes in the penetration depth influence the equivalent relative permeability as well. The relation between the penetration depth and the equivalent relative permeability is depicted in Figure 4. As the secondary frequency decreases, the penetration depth increases. Therefore, the equivalent relative permeability increases as well. Additionally, the penetration depth shows regular variation along with the speed and the variation equivalent relative permeability against speed which is observed to be slight between zero and synchronous speed.

At each iteration of the algorithm, the change in the equivalent permeability value of the secondary iron is calculated to be so small that current slip value in the iteration is nearly the same with the previous one, until speed approaches near the synchronous speed. Note that the linear speed is obtained by multiplying the synchronous speed ($2f\tau$) with the expression 1-s, where s denotes the slip value.

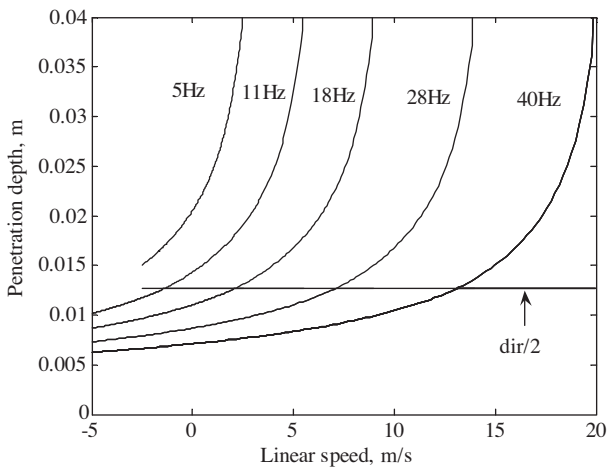

Figure 3. Penetration depth versus linear speed at different constant input frequencies.

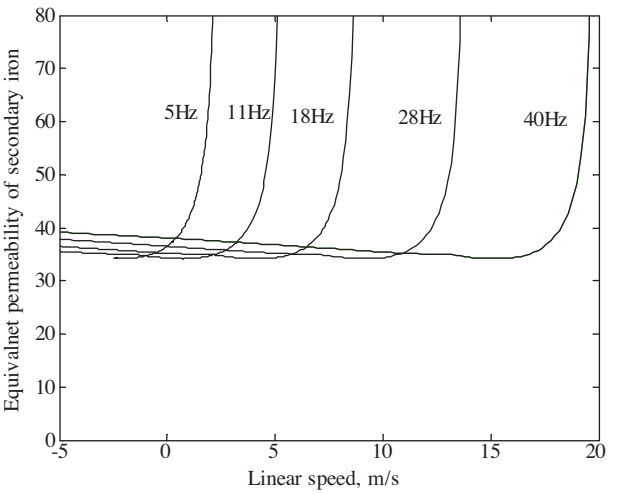

Figure 4. Variation of the equivalent permeability vs. linear speed at different input frequencies.

6. Obtaining the secondary impedance of SLIM in ECT

By solving the electromagnetic field equation which is obtained from the electromagnetic analysis by using the layering method, the following secondary iron layer impedance, aluminum layer impedance and magnetizing reactance equations are obtained respectively [3]:

$$Z_{Fe} = -\frac{j2\pi f s\mu_0\mu_{re}}{K_1}k_z \tag{20}$$

$$Z_{Al} = \frac{-j2\pi f s\mu_0}{K_2\tanh\left(K_2 d_{a1}\right)} \tag{21}$$

$$Z_m = -jX_m = -\frac{j2\pi f s\mu_0}{\beta\tanh\left(\beta g'\right)}. \tag{22}$$

The secondary iron layer impedance depends on the equivalent permeability, as shown in (20). The secondary iron impedance is calculated by considering variations of the equivalent permeability with the slip. This novel approach, which aims to calculate the secondary iron impedance with more sensitivity by utilizing a linear approximation method, is given in this section.

Together with the following approximation (such as $K_1 = \alpha_1,\ \tanh\left(K_2 d_{a1}\right) = K_2 d_{a1}$), the secondary iron layer and aluminum layer impedance equation for the above mentioned purpose can be written as

$$Z_{Al} = \frac{-j2\pi f s\mu_0}{K_2^2 d_{Al}}, \tag{23}$$

$$\begin{bmatrix} Z_{Fe}(s_0) \\ Z_{Fe}(s_1) \\ Z_{Fe}(s_2) \\ Z_{Fe}(s_3) \\ \vdots \\ Z_{Fe}(s_{\max}) \end{bmatrix} = -j2\pi\mu_0 k_z \begin{bmatrix} \frac{s_0 f}{\alpha_2(s_0)}\mu_{re}(s_0) & 0 & 0 & 0 & 0 & 0 \\ \frac{s_1 f}{\alpha_2(s_1)}\mu_{re}(s_0) & \frac{s_1 f}{\alpha_2(s_1)}\mu_{re}(s_1) & 0 & 0 & 0 & 0 \\ \frac{s_2 f}{\alpha_2(s_2)}\mu_{re}(s_0) & \frac{s_2 f}{\alpha_2(s_2)}\mu_{re}(s_1) & \frac{s_2 f}{\alpha_2(s_2)}\mu_{re}(s_2) & 0 & 0 & 0 \\ \frac{s_3 f}{\alpha_2(s_3)}\mu_{re}(s_0) & \frac{s_3 f}{\alpha_2(s_3)}\mu_{re}(s_1) & \frac{s_3 f}{\alpha_2(s_3)}\mu_{re}(s_2) & \frac{s_3 f}{\alpha_2(s_3)}\mu_{re}(s_3) & 0 & 0 \\ \vdots & \vdots & \vdots & \vdots & \vdots & \vdots \\ \frac{s_{max} f}{\alpha_2(s_{max})}\mu_{re}(s_0) & \frac{s_{max} f}{\alpha_2(s_{max})}\mu_{re}(s_1) & \frac{s_{max} f}{\alpha_2(s_{max})}\mu_{re}(s_2) & \frac{s_{max} f}{\alpha_2(s_{max})}\mu_{re}(s_3) & \cdots & \frac{s_{max} f}{\alpha_2(s_{max})}\mu_{re}(s_{max}) \end{bmatrix} \tag{24}$$

In order to take transverse edge effect into account, the impedance of secondary iron is multiplied by [8]

$$k_z = 1 - \frac{g}{L} + \frac{2}{\pi}\frac{\tau}{W}\left[1 - \exp\left(-\frac{\pi}{2}\frac{W}{L}\right)\right]. \tag{25}$$

In (24), each column vector represents the secondary iron layer impedance which corresponds to each slip value that is between zero and an appropriate value (1 or 2). The length of the column vector depends on the step value of slip. Consequently, maximum length of the column vector (l) can be defined as

$$l = \frac{s_{\max} - s_0}{step\ value}, \tag{26}$$

where s_0 denotes the minimum value of the slip and $s_{\max}$ stands for the maximum value of the slip that this value is chosen as 2 in this study.

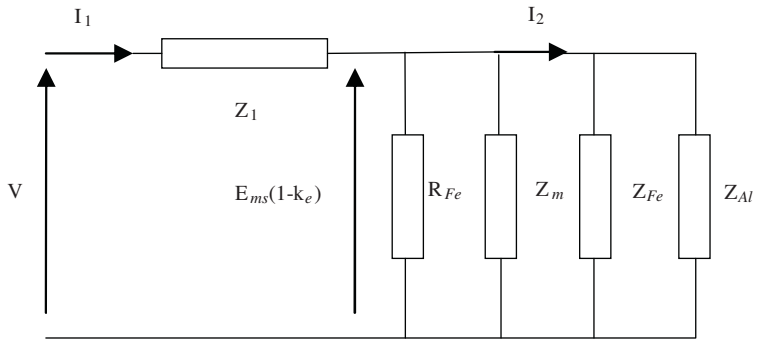

Figure 5. Per-phase equivalent circuit of SLIM.

Figure 5 depicts the T-type equivalent circuit of the SLIM with double-layer secondary where aluminum and secondary iron layer impedances are connected in parallel. Hence, equivalent secondary impedance referred to primary winding can be found by using classical circuit theory as

$$Z_2(s_n) = \frac{Z_{Fe}(s_n) Z_{Al}(s_n)}{Z_{Fe}(s_n) + Z_{Al}(s_n)} k_{tr} \frac{L}{\tau} \tag{27}$$

where

$$k_{tr} = \frac{2m\left(Nk_w\right)^2}{p} \text{ and } n = 0, 1, 2, \ldots, l.$$

The equivalent secondary impedance depends on the slip and should be determined for each slip value in the case of the different operating conditions. To do this, each column vector obtained from (23) is substituted into (26). However, it is not appropriate to calculate the secondary equivalent impedance in this way due to the mathematical constraints. After some required algebraic manipulation, the secondary impedance model assumes the form

$$A^n y = d^n \tag{28}$$

where

$$A^n = \left(X^n + \frac{s_n f}{K_2(n)\, d_{Al}} \right) \text{ and } d^n = \frac{-j2\pi\mu_0 X^n \left(s_n f\right)^2}{K_2^2(n)\, d_{Al}} k_{tr} \frac{L}{\tau},$$

and where X^n represents each column vector obtained from the equation (24) and y is the equivalent secondary impedance value. The column vector X^n, which actually holds secondary impedance values for each slip, can be shown as

$$Z_{Fe}(s_n) = X^n. \tag{29}$$

So, this model represents the secondary impedance and can now be evaluated by the least squares solution for the equivalent secondary impedance. To utilize the least squares solution, A^n, which represents column vector, should be transposed. Then the following relation is obtained to solve the y value that stands for the secondary impedance by the use of a least squares solution:

$$y = \left(\left(A^n\right)^T A^n \right)^{-1} \left(A^n\right)^T d^n. \tag{30}$$

The rest of the parameters required to evaluate equivalent circuit technique, i.e., the specific primary iron losses, primary impedance and air gap voltage, should be obtained. The specific primary iron core loss, which

is represented with R_{Fe}, is characterized by the equation

$$R_{Fe} = \frac{mE^2}{\Delta P_{Fe}} k_{ad}, \tag{31}$$

where ΔP_{Fe} is the core loss of the primary. On the other hand, the other required parameter, i.e., the primary impedance, Z_1, is calculated with the same way as in the rotary induction motor. As for the air gap voltage, which has to be calculated to take the end effect into account, the air gap voltage is obtained and multiplied by 1-k_e.

Thus, to validate of the proposed method, the steady-state thrust of the SLIM is calculated to compare the experimental results where the calculation is carried out by using the following equations:

$$F_x(s_n) = \frac{mR_2'(s_n)\left[I_2'(s_n)\right]^2}{s_n V s}, \tag{32}$$

where

$$R_2'(s_n) = \text{real}(y), \tag{33}$$

$$I_2'(s_n) = \frac{E\,(1-k_e)}{y}. \tag{34}$$

7. Conclusions and remarks

This study attempts to develop a new approach to obtain the secondary impedance of the SLIM. Section 6 presents the details of the novel approach and the present section looks at the relationship between the obtained secondary impedance with speed and thrust variations as a consequence of the adequate treatment of the saturation effect and permeability.

The relevancy between the secondary impedance, which is obtained by using the proposed approach, and speed is depicted in Figure 6. As can be seen in the figure, when approaching the synchronous speed, the secondary impedance stays nearly constant; however, it decreases sharply near the synchronous speed. This is an expected effect of the wave impedance concept since the change in the permeability of the iron is minimal until the penetration depth reaches the half of the thickness of the iron. When the penetration depth exceeds the half of the thickness and approaches the exact thickness of the iron, a decrease in the secondary impedance initiates. Once the penetration depth reaches the exact thickness of the iron, a sharp decrease occurs.

Since the secondary impedance is not a value that can be measured during the operation of the SLIM, thrust value should be employed in evaluation of the secondary impedance. As a result, the proposed approach can only be validated through the thrust values of the SLIM. Figure 7 depicts the curves of thrust values according to linear speed for constant frequency, e.g., 5 Hz, 11 Hz, 18 Hz, 28 Hz and 40 Hz. The obtained values as a result of the proposed method are compared to the experimental results of the CIGGT SLIM study [1] under different input frequencies. The results of proposed method are observed to be in accordance with the results of the CIGGT SLIM. Notice that, as seen in the figure, there is a good match between the objective model and the result of the proposed method at 40 Hz frequency. As far as similar studies in the literature are concerned, to the authors' knowledge, the proposed approach is the most efficient method studied in this frequency while it sacrifices computational speed on behalf of a more precise performance.

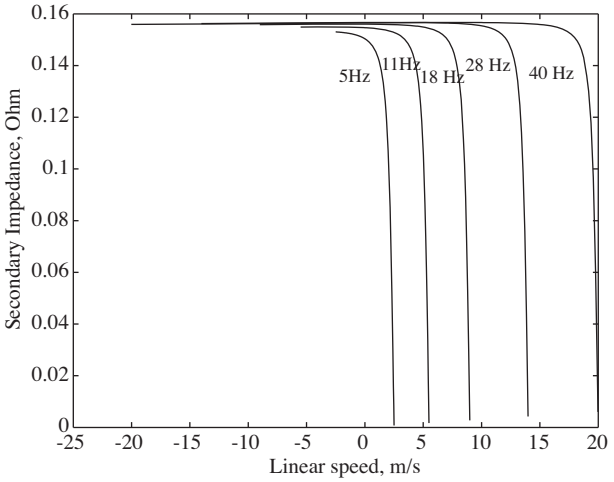

Figure 6. Secondary impedance vs. linear speed of CIGGT SLIM.

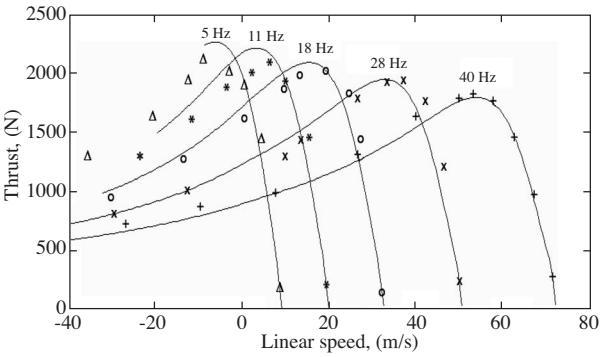

Figure 7. Simulation results for performance of the CIGGT SLIM; thrust as a function of linear speed. Experimental points: (+) denotes data for constant frequency of 40 Hz; (x) 28 Hz; (o) 18 Hz; (*) 11 Hz; and (Δ) denotes 5 Hz.

Faiz and Jafari [1] is one literature example that has attempted to develop analytical models to predict the sensitivity of the performance characteristics to parameters. In their paper, they consider end effects and equivalent thickness to find optimized parameters when analyzing SLIM performance characteristics. The paper reports that their proposed method outperforms two conventional methods in terms of SLIM performance analysis. One method compared with theirs was equalization of real parts of iron and aluminum with real part of hypothetical layer impedance with thickness dR'. However, our study shows that consideration of secondary iron impedance with modifications (i.e., utilizing linear approximation when calculating secondary iron impedance) has potential to outperform their methods, and is mainly related to the end effect and equivalent thickness (dR'). Figure 8 depicts this fact by including performance characteristics of this method, our method and CIGGT model.

Figure 8 shows curves describing values of thrust as a function of linear speed for constant frequencies, e.g., 5 Hz, 11 Hz, 18 Hz, 28 Hz and 40 Hz, where experimental results at each frequency is given with a separate symbols; circles correspond to the results at 5 Hz, plus signs denote 11 Hz, crosses denote18 Hz, stars for 28 Hz, and circled-plus signs for 40 Hz data. The dashed lines represent the results of our method and straight lines correspond to the results of the CIGGT SLIM study [1] from the literature. As the figure is examined, the dashed lines (our method) are closer to experimental model data (circled-plus) (CIGGT model) than the results of the study [1] (straight lines).

Another method from the literature similar to our method is the study by Gieras et al [3]. Their algorithm resembles ours in many ways, except calculation of the secondary impedance. With the modification in the secondary impedance calculation, our method outperforms their proposed method at higher frequencies, particularly at 40 Hz. However, as far as their results reported in the paper are concerned, performance analysis of our method at relatively lower frequencies is poorer than theirs. Thus, it can be concluded that our approach, which adopts linear approximation, has tendency to fail in lower frequencies due to rapid nonlinear change in speed-permeability curve (see Figure 4). Performance prediction our method at lower frequency can be considered as disadvantage of the method.

As a result, this paper introduced a new approach that might be efficient when used for design and analysis of the SLIM with a wide-range of applications by adequately treating the electromagnetic phenomena. The novel contribution of this paper is the utilization of the least squares approach for linear approximation in order to calculate the secondary impedance. The simulation results suggest that the proposed approach is efficient to improve the accuracy in thrust performance calculations. Since the proposed method is observed to be computationally intense, future studies of the method will include the evaluation of the optimization techniques to overcome this disadvantage.

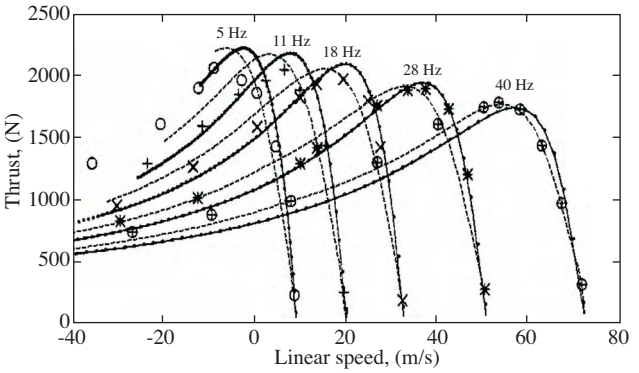

Figure 8. Comparison of simulation results with the performance of the CIGGT-SLIM.

Nomenclature

J_{ex}	Line current density	k_{tr}	Transverse edge factor
g	Air gap	L	Width of the primary core
d_{al}	Aluminum thickness	a_R	Coefficient for resistance and active power losses
d_{ir}	Back iron thickness	a_x	Coefficient for reactance and reactive power losses
σ_0	Conductivity of air gap	δ_{Fe}	Depth of penetration in back iron
μ_0	Permeability of air gap	A_m	Peak value of line current density of primary
σ_{Al}	Conductivity of Aluminum	N	Number of turn per phase
σ_{Fe}	Conductivity of the back iron	I	Primary current
μ_{Fe}	Permeability of the back iron	p	Number of pole pair
ω	Angular frequency of primary current	β	Real constant
k_{RN}	Russell and Norsworthy factor	α_1	Length of the penetration of entry-end effect wave
δ	Phase angle between the normal travelling field and the end effect wave	α_2	Length of the penetration of exit-end effect wave
τ_e	Pole pitch for end effect wave	f	Input frequency
τ	Pole pitch of the primary winding surface	H_x	x-axis magnetic field intensity
B_{ms}	Air-gap flux density wave due to fundamental wave	H_y	y-axis magnetic flux intensity
B_{me}	Air-gap flux density wave due to end-effect wave	M	Denominator in electromagnetic field equations
E_{ms}	Maximum value of induced electro-motive force by fundamental wave	Z_{Fe}	Impedance of Back iron
E_{me}	Maximum value of the induced electromotive force by the entry end effect wave wave	k_z	Transverse edge-effect factor
k_e	End effect factor	Z_{Al}	Impedance of Aluminum layer

k_{we}	Winding factor due to end wave	Z_m	Impedance of magnetizing branch
t_e	Attenuation factor	X_m	Reactance of magnetizing branch
μ_{re}	Equivalent permeability of the back iron	K_2	Propagation constant for back iron
μ_{rs}	Surface value of the relative permeability	K_1	Propagation constant for Aluminum
I_2'	Secondary current referred to the primary winding	R_{Fe}	Equivalent Resistance of the core losses
V_s	Synchronous speed	ΔP_{Fe}	Primary core loss
R_2'	Secondary resistance referred to primary winding	F_x	Thrust
k	Wave number	E	Induced voltage in primary phase
By	y-axis magnetic flux density	d_{av}	Average penetration distance in back iron
kc	Carter's coefficient	$k\mu$	Saturation factor
kw	Winding factor	s	Slip
sn	Slip value at n^{th} iteration	m	Number of phase
λ	Wavelength	W	Width of the primary

Acknowledgement

The authors would like to thank to TÜBİTAK for the support given this project under grant number 104M276.

References

[1] J. Faiz and H. Jafari, "Accurate Modeling of Single-Sided Linear Induction Motor Considers End Effect and Equivalent Thickness," IEEE Transaction on Magnetics, Vol. 36, pp. 3785–3790, 2000.

[2] M. Mirsalim, A. Doroudi and J. S. Moghani, "Obtaining the Operating Characteristics of Linear Induction Motors: A New Approach," IEEE Transaction on Magnetics, Vol. 38, pp. 1365–1370, 2002

[3] J. F. Gieras, G. E. Dawson and a. R. Eastham, " Performance Calculation for Single-Sided Linear Induction Motors with a Double-Layer Reaction Rail Under Constant current Excitation," IEEE Transaction on Magnetics, Vol. 22, pp. 54–62, 1986.

[4] R. M. Pai, I. Boldea and S. A. Nasar, " A Complete Equivalent Circuit of a Linear Induction Motor with Sheet secondary," IEEE Transaction on Magnetics, Vol. 24, pp. 639–654, 1988.

[5] R. M. Pai, S. A. Nasar and I. Boldea, "A Hybrid Method of Analysis of Low-Speed Linear Induction Motors," IEEE Transaction on Magnetics, Vol. 23, pp. 3908–3915, 1987.

[6] I. Boldea and M. Babescu "Multilayer approach to the analysis of single-sided linera induction motor," Proc. IEE, Vol. 125, pp. 283–287, 1978.

[7] R. L. Russell and K. M. Norsworthy, "Eddy Currents and Wall Losses in Screened Rotor Induction Motors," *Proc. IEE,* Vol. 105A, pp. 163–175, 1958.

[8] J. F. Gieras, G. E. Dawson and A. R. Eastham, "A New Longitudinal End Effect Factor for Linear Induction Motors," IEEE Transactions on Energy Conversion, Vol. EC-2, pp. 152–159, 1987.

[9] J. F. Gieras, A. R. Eastham and G. E. Dawson, "Performance Calculation for single-sided Linear Induction Motors with a Solid steel Reaction Plate Under Constant Current Excitation," IEE Proceedings, Vol. 132, pp.185–194, 1985.

[10] J. F. Gieras, "Analytical Method of Calculating the Electromagnetic Field and Power Losses in Ferromagnetic Half Space, Taking into Account Saturation and Hysteresis," In Proceedings of IEE, Vol. 124, pp. 1098–1104, 1977.

[11] J. F. Gieras, G. E. Dawson and A. R. Eastham, " The Influence of Conductive Cap Thickness on the Performance of Single-Sided Linear Induction Motors," Electric Machines and Power Systems, Vol. 11, pp. 125–136, 1986.

[12] J. F. Gieras, Linear Induction Drives, Clarendon Press, Oxford, 1994.